Nanophotonic resonators for InP solar cells

Daniel A. Goldman,[1,2] Joseph Murray,[1,2] and Jeremy N. Munday[1,2,*]

[1]*Department of Electrical and Computer Engineering, University of Maryland, College Park, MD, 20742, USA*
[2]*Institute for Research in Electronics and Applied Physics, University of Maryland, College Park, MD, 20742, USA*
[*]*jnmunday@umd.edu*

Abstract: We describe high efficiency thin-film InP solar cells that utilize a periodic array of TiO_2 nanocylinders. These nanophotonic resonators are found to reduce the solar-weighted average reflectivity of an InP solar cell to ~1.3%, outperforming the best double-layer antireflection coatings. The coupling between Mie scattering resonances and thin-film interference effects accurately describes the optical enhancement provided by the nanocylinders. The spectrally resolved reflectivity and *J-V* characteristics of the device under AM1.5G illumination are determined via coupled optical and electrical simulations, resulting in a predicted power conversion efficiency > 23%. We conclude that the nanostructured coating reduces reflection without negatively affecting the electronic properties of the InP solar cell by separating the nanostructured optical components from the active layer of the device.

References and links

1. K. Jäger, M. Fischer, R. A. C. M. M. van Swaaij, and M. Zeman, "A scattering model for nano-textured interfaces and its application in opto-electrical simulations of thin-film silicon solar cells," J. Appl. Phys. **111**(8), 083108 (2012).
2. M. Boccard, C. Battaglia, S. Hänni, K. Söderström, J. Escarré, S. Nicolay, F. Meillaud, M. Despeisse, and C. Ballif, "Multiscale Transparent Electrode Architecture for Efficient Light Management and Carrier Collection in Solar Cells," Nano Lett. **12**(3), 1344–1348 (2012).
3. M. L. Brongersma, Y. Cui, and S. Fan, "Light management for photovoltaics using high-index nanostructures," Nat. Mater. **13**(5), 451–460 (2014).
4. C. E. R. Disney, S. Pillai, C. M. Johnson, and M. A. Green, "Self-Assembled Nanostructured Rear Reflector Designs for Thin-Film Solar Cells," ACS Photonics **2**(8), 1108–1116 (2015).
5. L. Zeng, P. Bermel, Y. Yi, B. A. Alamariu, K. A. Broderick, J. Liu, C. Hong, X. Duan, J. Joannopoulos, and L. C. Kimerling, "Demonstration of enhanced absorption in thin film Si solar cells with textured photonic crystal back reflector," Appl. Phys. Lett. **93**(22), 221105 (2008).
6. P. Bermel, C. Luo, L. Zeng, L. C. Kimerling, and J. D. Joannopoulos, "Improving thin-film crystalline silicon solar cell efficiencies with photonic crystals," Opt. Express **15**(25), 16986–17000 (2007).
7. J. N. Munday and H. A. Atwater, "Large integrated absorption enhancement in plasmonic solar cells by combining metallic gratings and antireflection coatings," Nano Lett. **11**(6), 2195–2201 (2011).
8. H. R. Stuart and D. G. Hall, "Absorption enhancement in silicon-on-insulator waveguides using metal island films," Appl. Phys. Lett. **69**(16), 2327–2329 (1996).
9. V. E. Ferry, J. N. Munday, and H. A. Atwater, "Design considerations for plasmonic photovoltaics," Adv. Mater. **22**(43), 4794–4808 (2010).
10. K. R. Catchpole and A. Polman, "Plasmonic solar cells," Opt. Express **16**(26), 21793–21800 (2008).
11. R. Santbergen, H. Tan, M. Zeman, and A. H. M. Smets, "Enhancing the driving field for plasmonic nanoparticles in thin-film solar cells," Opt. Express **22**(S4), A1023–A1028 (2014).
12. P. Spinelli, M. A. Verschuuren, and A. Polman, "Broadband omnidirectional antireflection coating based on subwavelength surface Mie resonators," Nat. Commun. **3**, 692 (2012).
13. F. J. Bezares, J. P. Long, O. J. Glembocki, J. Guo, R. W. Rendell, R. Kasica, L. Shirey, J. C. Owrutsky, and J. D. Caldwell, "Mie resonance-enhanced light absorption in periodic silicon nanopillar arrays," Opt. Express **21**(23), 27587–27601 (2013).
14. D. Shir, J. Yoon, D. Chanda, J. H. Ryu, and J. A. Rogers, "Performance of ultrathin silicon solar microcells with nanostructures of relief formed by soft imprint lithography for broad band absorption enhancement," Nano Lett. **10**(8), 3041–3046 (2010).

15. P. Spinelli and A. Polman, "Light Trapping in Thin Crystalline Si Solar Cells Using Surface Mie Scatterers," IEEE J. Photovoltaics **4**(2), 554–559 (2014).
16. M. A. Green, "Radiative efficiency of state-of-the-art photovoltaic cells," Prog. Photovolt. Res. Appl. **20**(472), 6–11 (2012).
17. I. Schnitzer, E. Yablonovitch, C. Caneau, and T. J. Gmitter, "Ultrahigh spontaneous emission quantum efficiency, 99.7% internally and 72% externally, from AlGaAs/GaAs/AlGaAs double heterostructures," Appl. Phys. Lett. **62**(2), 131–133 (1993).
18. O. D. Miller, E. Yablonovitch, and S. R. Kurtz, "Intense internal and external fluorescence as solar cell approach the SQ efficiency limit," IEEE J. Photovoltaics **2**(3), 1–27 (2012).
19. D. E. Aspnes and A. A. Studna, "Dielectric functions and optical parameters of Si, Ge, GaP, GaAs, GaSb, InP, InAs, and InSb from 1.5 to 6.0 eV," Phys. Rev. B **27**(2), 985–1009 (1983).
20. M. A. Green, K. Emery, Y. Hishikawa, W. Warta, and E. D. Dunlop, "Solar cell efficiency tables (version 46)," Prog. Photovolt. Res. Appl. **23**(7), 805–812 (2015).
21. B. M. Kayes, H. Nie, R. Twist, S. G. Spruytte, F. Reinhardt, I. C. Kizilyalli, and G. S. Higashi, "27.6% Conversion efficiency, a new record for single-junction solar cells under 1 sun illumination," in *Conference Record of the Thirty Second IEEE Photovoltaic Specialists Conference* (IEEE, 2011), pp. 000004–00008.
22. C. J. Keavney, V. E. Haven, and S. M. Vernon, "Emitter Structures in MOCVD InP Solar Cells," in *Conference Record of the Twenty First IEEE Photovoltaic Specialists Conference* (IEEE, 1990), pp. 141–144.
23. Y. Xu, T. Gong, and J. N. Munday, "The generalized Shockley-Queisser limit for nanostructured solar cells," Sci. Rep. **5**, 13536 (2015).
24. Y. Da and Y. Xuan, "Role of surface recombination in affecting the efficiency of nanostructured thin-film solar cells," Opt. Express **21**(S6), A1065–A1077 (2013).
25. N. Huang, S. Member, and M. L. Povinelli, "Design of Passivation Layers on Axial Junction GaAs Nanowire Solar Cells," IEEE J. Photovoltaics **4**(6), 1511–1517 (2014).
26. B. Rastegar and J. F. Wager, "Surface recombination velocity and bulk lifetime in GaAs and InP," Semicond. Sci. Technol. **1**(3), 207–212 (1986).
27. J. Wallentin, N. Anttu, D. Asoli, M. Huffman, I. Aberg, M. H. Magnusson, G. Siefer, P. Fuss-Kailuweit, F. Dimroth, B. Witzigmann, H. Q. Xu, L. Samuelson, K. Deppert, and M. T. Borgström, "InP nanowire array solar cells achieving 13.8% efficiency by exceeding the ray optics limit," Science **339**(6123), 1057–1060 (2013).
28. M. T. Borgström, J. Wallentin, M. Heurlin, S. Fält, P. Wickert, J. Leene, M. H. Magnusson, K. Deppert, and L. Samuelson, "Nanowires with promise for photovoltaics," IEEE J. Sel. Top. Quantum Electron. **17**(4), 1050–1061 (2011).
29. N. M. Shmidt, "Indium Phosphide (InP)," in *Handbook Series on Semiconductor Parameters,* vol. 1, M. Levinshtein, S. Rumyantsev, and M. Shur, eds. (World Scientific, 1996).
30. J. R. DeVore, "Refractive Indices of Rutile and Sphalerite," J. Opt. Soc. Am. **41**(6), 416–419 (1951).
31. Y. Lin, R. Kapadia, J. Yang, M. Zheng, K. Chen, M. Hettick, X. Yin, C. Battaglia, I. D. Sharp, J. W. Ager, and A. Javey, "Role of TiO2 Surface Passivation on Improving the Performance of p-InP Photocathodes," J. Phys. Chem. C **119**, 2308 (2015).
32. X. Yin, C. Battaglia, Y. Lin, K. Chen, M. Hettick, M. Zheng, C. Y. Chen, D. Kiriya, and A. Javey, "19.2% Efficient InP Heterojunction Solar Cell with Electron-Selective TiO2 Contact," ACS Photonics **1**(12), 1245–1250 (2014).
33. P. Spinelli, B. Macco, M. A. Verschuuren, W. M. M. Kessels, and A. Polman, "Al2O3/TiO2 nano-pattern antireflection coating with ultralow surface recombination," Appl. Phys. Lett. **102**(23), 10–13 (2013).
34. D. Maystre, *Plasmonics: From Basics to Advanced Topics* (Springer, 2012), Chap. 2.
35. P. Spinelli, F. Lenzmann, A. Weeber, and A. Polman, "Effect of EVA Encapsulation on Antireflection Properties of Mie nanoscatterers for c-Si Solar Cells," IEEE J. Photovoltaics **5**(2), 559–564 (2015).

1. Introduction

Thin-film photovoltaics have provided a critical design avenue to help decrease the overall cost of solar power. However, a major drawback of thin-film solar cell technology is decreased optical absorption, making compact, high-quality anti-reflection coatings of critical importance to ensure that all available light enters the cell. Various photonic designs have been utilized to raise the efficiency of these cells beyond the enhancement provided by traditional thin-film dielectric antireflection coatings (ARCs), including nano-textured transparent conducting oxides (TCOs) [1,2], nanostructured dielectric reflectors [3–6], plasmonic structures [7–11], etc. The success and limitations of these strategies (including parasitic absorption and wavelength and angle sensitivity) only further emphasizes the need to take advantage of other optical mechanisms to increase absorption in thin-film solar cells.

A recently proposed novel antireflection and photonic design concept was suggested using a periodic square array of subwavelength nanocylinders (NCs) on silicon (Si) [12]. These structures utilize Mie resonances, which couple to leaky optical modes in the high-index Si

substrate, reducing the reflectance of the device to less than 8% over the entire spectral range [12]. Resonances in the Si nanostructures have been found to exhibit strong dependences on different geometric parameters such as nanocylinder diameter and array period [13]. Additional studies have shown that these types of nanostructures can be fabricated via inexpensive processes such as nanoimprint lithography, and exhibit significant light absorption enhancement in thin-film silicon solar cells [14,15]. While these nanostructures and design techniques have yielded substantial improvements for Si, thin-film III-V photovoltaics with thicknesses < 1 μm offer the possibility of even higher efficiencies. III-V materials, though expensive to manufacture, offer significant benefits such as radiatively limited recombination [16–18], large absorption coefficients [19], high conversion efficiencies [20–22], and the possibility of built-in optical concentration [23]. The large absorption coefficients of direct bandgap III-V materials such as gallium arsenide (GaAs) and indium phosphide (InP) result in higher absorption using less material. Thus, nanoscale optical coatings may result in similar performance enhancements using even thinner layers than can be achieved with Si-based devices; however, a potential disadvantage of nanostructuring is the possibility of increased non-radiative recombination processes [24,25].

Because nanostructuring a material results in increased surface area and possibly substantial surface damage, the potential avenues for surface recombination to occur increase dramatically with surface nanostructuring. Though GaAs is the prototypical III-V photovoltaic material due to its ideal bandgap and high conversion efficiency, InP has the potential to perform similarly well and has a lower surface recombination velocity [26]. This quality makes InP an excellent candidate to explore nanostructured photovoltaic design concepts, and InP nanowire-based photovoltaic devices have already demonstrated great promise [27,28]. Here we show that InP solar cells with nanostructured coatings can outperform devices with traditional thin-film antireflection coatings through a combination of scattering resonances and thin-film interference effects. Further, we show that the device can perform as well as advanced multilayer ARCs, but without the need for multilayer coatings. Finally, we find that a nanostructured TiO_2 film can further reduce reflection below that of a device consisting only of InP, enabling a nanophotonic coating that does not affect the electronic properties of the underlying material.

2. Nanophotonic resonators for InP

A simple nanophotonic structure made completely of InP is shown in Fig. 1(a). We perform three-dimensional finite difference time domain (FDTD) simulations to calculate the reflection and quantify the optical performance of these nanophotonic resonant structures. The structure is illuminated with normally incident light from a broadband ($\lambda = 350$ nm to 925 nm) plane wave optical source, corresponding to the above bandgap components of the solar spectrum for InP. For all of our simulations, we assume ambient room temperature conditions (T = 300K), which we used to obtain our value for the cutoff wavelength for InP [29]. We define a simulation region based on the specific geometry of the nanocylinders (periodicity and height). A single unit cell is simulated, with periodic boundary conditions to replicate the periodic square array of nanocylinders. Periodic hexagonal arrays of these structures were also investigated, but the results had negligible deviations from the square array results, leading us to focus on square arrays for simplicity. We use a perfectly matched layer (PML) boundary condition at the bottom of the simulation volume to simulate an infinitely thick layer of InP, which allows us to study only the coupling of the incident light into the InP without additional effects due to light reflection off the back surface. Simulations of finite thickness samples in a device-like architecture are discussed in Section 4. In all of the simulations, the mesh size was refined until there was negligible change in the reflectance spectrum, typically less than a few hundredths of a percent (corresponding to mesh sizes ~1 nm). Wavelength-dependent optical data (n,k) was obtained from Ref [19]. for InP and Ref

[30]. for TiO_2. Over the relevant spectral range (λ = 350 nm to 925 nm), the real part of the refractive index is ~3.7 for InP and ~2.5 for TiO_2.

To determine the optimal geometries for the nanophotonic resonant structures, we perform parameter sweeps and find the minimized solar-weighted reflectivity. We calculate the solar-weighted reflectivity using the spectrally resolved reflectivity from the nanostructured solar cell, $R(\lambda)$, weighted by the solar photon flux from the AM1.5G spectrum at each wavelength, $\phi_{AM1.5G}(\lambda)$, which is integrated over the available wavelengths (λ_{min} = 350 nm to λ_g = 925 nm, the bandgap wavelength):

$$R_{AM1.5G} = \frac{\int_{\lambda_{min}}^{\lambda_g} R(\lambda)\phi_{AM1.5G}(\lambda)d\lambda}{\int_{\lambda_{min}}^{\lambda_g} \phi_{AM1.5G}(\lambda)d\lambda}. \qquad (1)$$

Using this figure of merit [Eq. (1)], we obtain contour plots of the solar-weighted reflectance as a function of nanocylinder diameter and period [Fig. 1(b)]. We performed these optimizations for four nanocylinder heights from 50 – 200 nm and found that InP nanocylinders with a height of 100 nm, diameter of 120 nm, and array period of 180 nm minimized the solar-weighted reflectance from the cell. We then calculated the electric field intensity profile for this optimized geometry (shown for an incident wavelength of λ = 458 nm in Fig. 1(c) – inset).

In order to quantitatively compare the optical performance of the nanostructures to current optical design methodologies, we perform reflectance simulations identical to those completed on the nanostructures with various antireflection coating materials [Fig. 1(c)]. For bare InP with no optical coating, the solar-weighted average reflectance is 37% and is much larger than any option with a coating. Silicon nitride (Si_3N_4) is a typical material used as a dielectric single-layer antireflection coating for photovoltaic cells. We find that the optimal thickness for this layer on our InP cells is 50 nm, which resulted in a solar-weighted average reflectance of 7.5%. However, our InP nanocylinder arrays perform even better than this antireflection coating, with a 3.7% solar-weighted average reflectance and significant reflectivity suppression throughout the visible. Two pronounced minima occur in the reflectance data for the InP NCs in Fig. 1(c). The minimum at λ = 458 nm shows strong forward scattering into the InP substrate as a result of a Mie-like resonance, while the minimum at λ = 599 nm results from a thin-film interference effect. Both the Mie resonance and thin-film interference effects are described in Section 3. These results provide strong evidence that optically designed nanostructures have significant potential as antireflection layers, and that this effect is not limited to Si but may be beneficial for many thin-film high index absorber materials, *e.g.* InP, GaAs, etc. For these direct bandgap materials, the anti-reflection properties of the nanostructures become more important than the light trapping properties because nearly 95% of the entering light (at λ = 900 nm) can be absorbed within a 1 μm InP cell with a back reflector. However, for a 1 μm Si cell with a back reflector to absorb a similar fraction of the above bandgap spectrum, a light trapping factor (*i.e.* path length enhancement) of 16 would be needed. Thus, for thin-film (~1 μm) direct bandgap semiconductors, the design of high quality anti-reflection coatings is of greater importance.
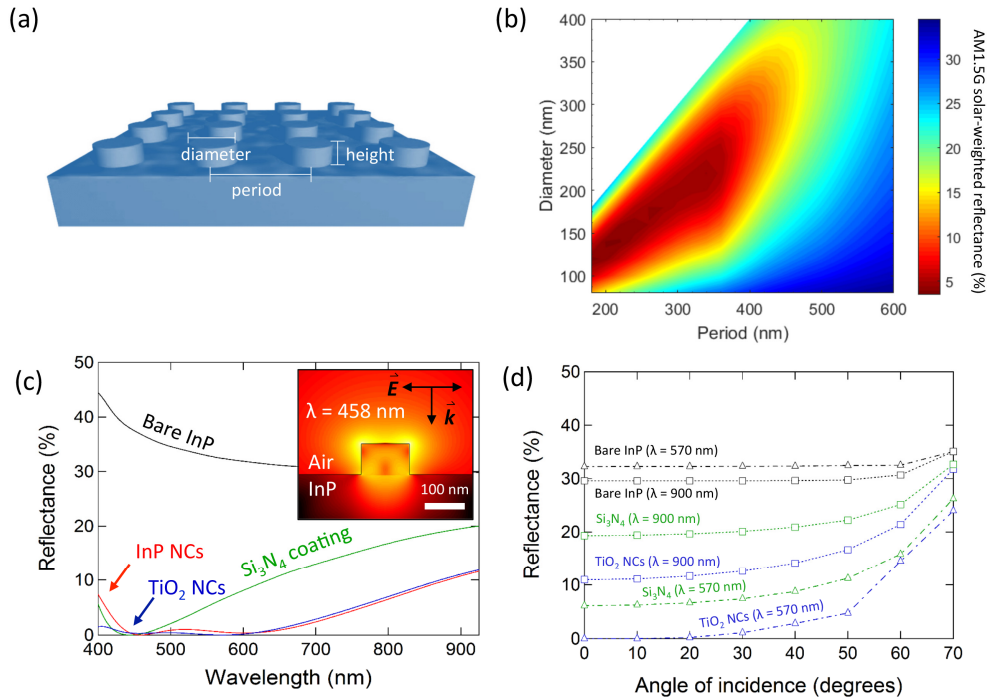
Fig. 1. Nanophotonic resonant structures in InP. (a) Schematic of the nanocylinder array in InP. (b) Contour map of the solar-weighted reflectivity of nanophotonic resonant structures in InP as a function of diameter and period. Results shown are for nanocylinders with a height of 100 nm. (c) Spectrally resolved reflectance for various coatings on InP: bare InP (black), a 50 nm Si_3N_4 ARC (green), optimized InP NCs (red), and optimized TiO_2 NCs (blue). Inset – Electric field intensity profile for optimized InP NCs at $\lambda = 458$ nm using a total-field scattered-field calculation. The field inside the nanocylinder is the total field (incident plus scattered) and the field outside of the nanocylinder is the scattered field. (d) Reflectance as a function of incident angle for bare InP (black), the 50 nm thick Si_3N_4 ARC (green) and the TiO_2 nanocylinder coating (blue) at $\lambda = 570$ nm (triangles, dashed lines) and $\lambda = 900$ nm (squares, dotted lines) averaged over both polarizations.

To avoid potentially increased surface recombination resulting from a textured active layer, we also explored the use of nanostructured titanium dioxide (TiO_2) coatings on InP solar cells as a means to maintain similar optical enhancement without negatively impacting the overall device performance. Further, it has been shown that TiO_2 is a highly effective passivating layer when used as a coating on InP [31], may be used as a highly efficient hole-selective contact [32], and provides substantial optical improvement when used as a nanostructured coating on Si [33]. We have also included a thin TiO_2 spacer layer separating the nanocylinders from the InP active layer, which would aid with surface passivation and improved optical performance in a fabricated device. By performing the same optimizations and analyses on these TiO_2 nanostructures as the InP nanostructures, we determined that a 30 nm thick spacer layer provides the lowest solar-weighted reflectance over the full spectral range regardless of nanocylinder geometry. These optimizations revealed that TiO_2 nanocylinders with a height of 100 nm, diameter of 180 nm, and array period of 320 nm minimize the solar-weighted reflectance, with a solar-weighted average reflectance of 1.3% over the spectral range [Fig. 1(c)], even surpassing the performance of the optimized dual layer ARC (3.1% solar-weighted average reflectance) used in the world record InP device [22]. Additionally, these coatings provide reduced reflection over a wide range of off-normal incidence angles [Fig. 1(d)].

3. Mechanisms for improved optical performance

We can gain more insight into the optical mechanisms behind the advantages of these TiO_2 nanostructures by considering the spectrally resolved reflectance as a function of diameter and period [Fig. 2]. Variations in the reflectance versus nanocylinder diameter can reveal information about localized modes in these structures, while pitch variations can uncover information about the coupling between different nanostructures as a result of grating and diffraction effects. There are two large regions of minimal reflectance (near $\lambda = 454$ nm and $\lambda = 570$ nm) for the optimized geometry, which can be explained by the combination of two different optical effects. The first is that of a Mie resonance, which originates at wavelengths between 400 and 450 nm for small nanocylinder diameters and intersects with the optimized geometry (denoted as dashed vertical lines in Fig. 2) at the first local minimum in the reflectance spectrum ($\lambda = 454$ nm). This resonance is verified by the field intensity profile shown in the inset. The field profile is qualitatively similar to that of Fig. 1(c) (for InP NCs) with two high intensity lobes at the top corners of the nanocylinder and strong forward scattering into the substrate. This is primarily the result of light from a Mie resonance in the nanostructure coupling into leaky optical modes in the high index InP substrate [12].
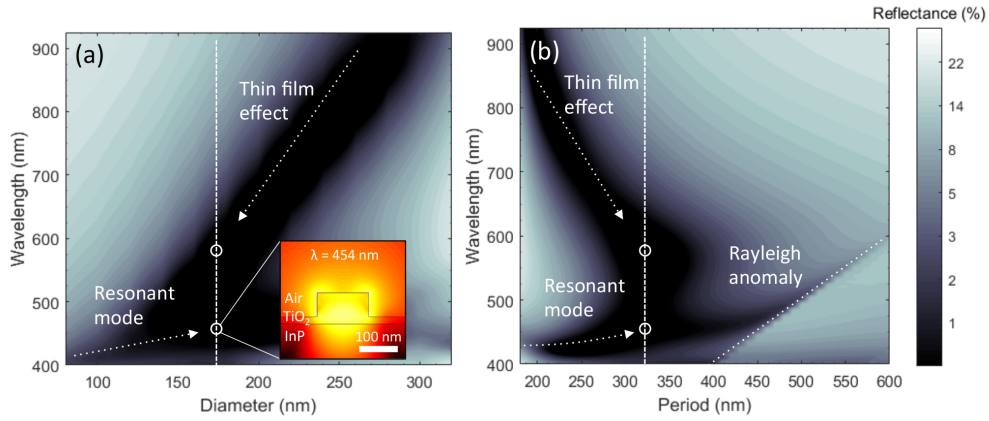

Fig. 2. Optical performance of TiO_2 nanophotonic resonant structures with a height of 100 nm on InP. (a) Reflectance of TiO_2 nanocylinders (NCs) on InP as a function of wavelength and diameter for a period of 320 nm. Inset – Electric field intensity profile for optimized TiO_2 NC structure. Electric field polarization and *k*-vector of incident light are identical to the inset of Fig. 1(c). (b) Reflectance of TiO_2 NCs on InP as a function of wavelength and array period for nanocylinders with a diameter of 180 nm. For (a) and (b) the dashed lines indicate the optimized structure, the circles indicate positions of local minima in the reflectance spectrum, and the dotted lines indicate spectral features that can be described by specific optical effects.

The second minimal reflectance region is seen near $\lambda = 570$ nm for the optimum geometry, which is more pronounced for diameters larger than the optimum (labeled as thin-film effect in Fig. 2(a)) and for array periods smaller than the optimum (labeled as thin-film effect in Fig. 2(b)). This minimal reflectance region can be attributed to a thin-film effect provided by the nanocylinders acting as a layer with an effective refractive index. The mixture of the high index TiO_2 nanocylinders and the surrounding air acts as a thin-film with a thickness governed by the nanocylinder height and an effective index that is calculated as a volume weighted average of the refractive indices of the two materials (TiO_2 and air):

$$n_{eff} = n_{TiO_2}\left(\frac{\pi d^2}{4p^2}\right) + n_{air}\left(1 - \frac{\pi d^2}{4p^2}\right),\qquad(2)$$

where n_{TiO2} is the refractive index of TiO$_2$, $n_{air} = 1$, d is the nanocylinder diameter, and p is the periodicity. In fact, the entire structure can be approximated as a dual layer ARC, with a top layer described by the effective index determined by the nanocylinders [Eq. (2)] and a bottom layer described by the TiO$_2$ spacer layer [Fig. 3]. To verify this effect, we ran optical simulations of a dual layer ARC with a top layer consisting of an effective index determined by [Eq. (2)] (representing the NCs) and a bottom layer of 30 nm of TiO$_2$ for the spacer layer. The results are shown in Fig. 3(a), which indicate clear quantitative and qualitative agreement with the data from Fig. 2(a), capturing the thin-film effect for long wavelengths and large NC diameters. For the optimized geometry [Fig. 3(b)], the dual layer ARC model accurately reproduced the long-wavelength broadband reflectance suppression while missing the short wavelength reflectance minimum due to the resonant mode.

While the strategy to reduce reflection via a combination of Mie resonances and thin-film coating effects is quite general, the refractive indices of the materials used in this study are particularly beneficial. On its own, TiO$_2$ (with a refractive index of ~2.5 over the visible spectrum) is not a great thin-film dielectric antireflection coating for InP due to its large index contrast with air. However, the inclusion of the NC coating layer (which has $n_{eff} = 1.39$ for the optimized structure), enables a graded index-like behavior. This combination of materials yields an index of refraction profile that more gradually transitions from air ($n_{air} = 1$) to InP ($n_{InP} = 3.7$) through the inclusion of two additional layers with $n_{eff} = 1.39$ and $n_{TiO2} = 2.5$, thus yielding a better impedance match between air and InP. Additionally, in Fig. 2(b) there is another unique spectral feature characterized by a reflectance minima at wavelengths equivalent to the array period. This feature is the consequence of a Rayleigh anomaly, which appears for similar structures on Si [12], and describes a dramatic change in the diffracted field from a grating as the result of a scattered wave emerging tangentially to the grating surface [34]. The scattered light traveling with a momentum in the plane of the nanocylinders is more strongly absorbed in the nanocylinders, causing the large reflectance dips in the spectrum at those specific wavelengths.
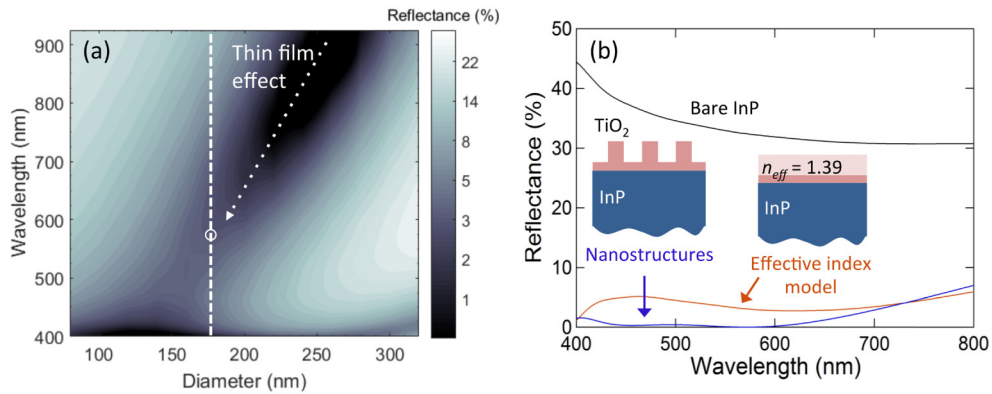

Fig. 3. Optical performance of TiO$_2$ nanophotonic resonant structures acting as a dual layer ARC with an effective index. (a) Reflectance of a dual layer ARC on InP as a function of wavelength and NC diameter for a period of 320 nm and height of 100 nm. The top layer has a thickness equivalent to the NC height and an effective index calculated using [Eq. (2)]. The bottom layer is the 30 nm thick TiO$_2$ spacer layer. For (a) the dashed line indicates the optimized structure, the circle indicates the position of a local minima from the original reflectance spectrum [Figs. 2(a)-2(b)], and the dotted lines indicate a spectral feature that can be described by a specific optical effect. (b) Comparison between the reflectance spectra for the optimized nanostructured device (NC height = 100 nm, period = 320 nm, NC diameter = 180 nm) and a simple effective index model for this optimized NC geometry.

4. Electrical simulations and device characteristics

In order to quantify the device performance enhancements resulting from our TiO_2 nanostructures, we use the results from the optical simulations as inputs in electrical device simulations to determine the expected power conversion efficiencies. For the optical simulations, we again use the FDTD method and vary the InP thicknesses, including an ideal metal back reflector. Using the spatially resolved absorption profile, the generation rate is calculated, assuming one electron-hole pair per absorbed photon [9]. This rate is used to determine the carrier dynamics in electrical device simulations using a finite-element based software platform (Lumerical DEVICE) to solve the semiconductor drift-diffusion equations. We design the photovoltaic device for these simulations using a nominal p-i-n structure for a solar cell, with a background p-doping concentration of 10^{15} cm^{-3} [Fig. 4]. The cell is illuminated from the top surface, which consists of an 80 nm thick doped n^+ (10^{19} cm^{-3}) InP layer. Below lies the intrinsic p-layer with the background concentration, which makes up the base, and finally another 80 nm thick doped InP layer, this time with p^+ (10^{19} cm^{-3}) doping [Fig. 4]. This doping profile is optimized within reasonable limits and based on the generation rates within the active InP layer obtained from the optical simulations (Lumerical FDTD). The optical data for these doped layers of InP is assumed to be the same as that of the intrinsic material. We assume ideal ohmic contacts at flatband voltage conditions, and the device model includes modest surface recombination velocities ($S = 10^7$ cm/s) at the interfaces between the active layer and the contacts [26]. The device simulations also incorporate radiative and non-radiative (Shockley-Read-Hall (SRH) and Auger) recombination mechanisms in the InP active layer. For SRH recombination we use a bulk minority carrier lifetime of 10^{-8} s in the p-doped base layer and 3 x 10^{-6} s in the n-doped emitter. We assume a radiative recombination rate of 2 x 10^{-10} cm^3/s and an Auger coefficient of 9 x 10^{-31} cm^6/s. All of the above values were obtained from Ref [29]. and were utilized to recreate the electronic conditions seen in a real device.

Optical simulations yield the generation rate profiles, integrated over the full spectrum to yield the number of electron-hole pairs generated per volume of InP per second [Figs. 4(a)-4(c)]. The three generation rate profiles shown were obtained for an InP layer thickness of 1 μm because they demonstrated the best optical and electrical performance, though simulations were performed for 0.5, 1, and 2 μm thick InP layers. The generation enhancement is clearly seen in these images, as the carrier generation, particularly in the top half-micron of InP, increases for the Si_3N_4 and TiO_2 NC coatings compared to the bare InP. In particular, the strong forward scattering of light from the TiO_2 nanostructures into the InP results in a high generation rate in the top half of the cell. The various minima in the lower half of the generation rate profiles are due to optical interference effects between the incident light and the reflected light from the back reflector. The calculated generation rate profiles are input into the electrical simulations, which calculate the specific solar cell device parameters as well as the J-V characteristics [Fig. 4(e)]. Table 1 summarizes the results of our device simulations for each thickness of the InP active layer.

The large short-circuit current density enhancement is clearly seen in the data, as expected due to antireflection effects provided by our nanostructured optical coating. The > 23% efficiency of this device is a result of improved current density and voltage in our proposed design while simultaneously reducing cell thickness. However, the parameters of our simulation define idealized conditions, namely an ideal back reflector, idealized contacts, perfect periodicity, and no damage to the device due to additional processing. Some of these conditions may be unable to be met in a fabricated device, which would likely reduce the power conversion efficiency. We also note that the slight improvement of the fill factor as the active layer thickness is reduced [Table 1] is likely due to improved carrier transport and collection. To further extend the practical implications of our design, we performed simulations to determine the effects of encapsulation of these cells in EVA (ethylene vinyl

acetate), the industry standard for encapsulants in commercial solar modules. Following the methodology outlined by Spinelli *et. al.* [35], we found that the solar-weighted average reflectance for our optimized structure increased from 1.3% at the air/TiO_2 interface to 5.1% at the EVA/TiO_2 interface, due in part to the onset of backscattered grating orders below wavelengths of 480 nm; however, this structure still outperforms a 50 nm planar Si_3N_4 coating, which has an average solar-weighted reflectivity of 7% (EVA/Si_3N_4 interface). An additional 4.4% reflection offset from the glass-air interface will also occur for both of these structures, as is typical for a module [35]. Further studies to optimize these nanostructures within an encapsulant could reveal the versatility of these types of nanophotonic coatings on different materials and in different optical environments. Overall, the thin-film devices with the nanostructured TiO_2 coatings show vastly improved performance compared to both the bare InP and the Si_3N_4 ARC.
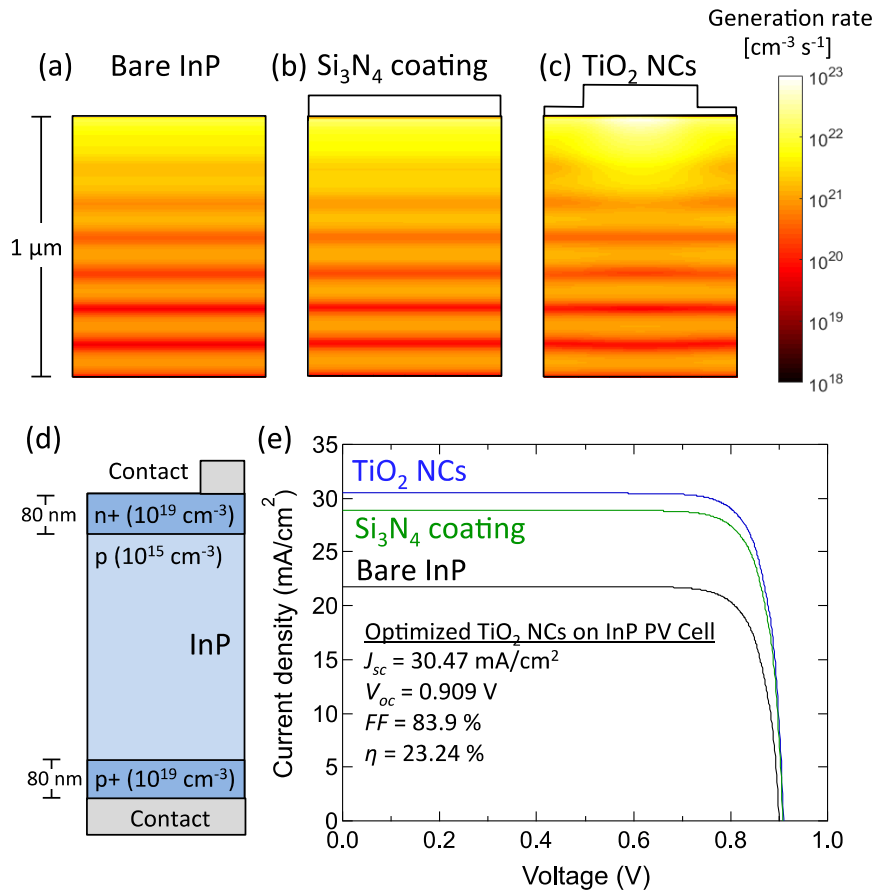

Fig. 4. Generation rate profiles and *J-V* curves for InP solar cells with various coatings. Generation rate profiles were calculated via optical simulations of 1 μm - thick InP solar cells with an ideal metal back reflector and different optical coatings: (a) Bare InP, (b) 50 nm of Si_3N_4, and (c) optimized TiO_2 NCs. (d) Device parameters for *p-i-n* cell. (e) *J-V* characteristics for InP cells using the above coatings: bare InP (black), Si_3N_4 (green), optimized TiO_2 NCs (blue). Significant current density enhancement is found for our optimized TiO_2 nanophotonic coatings.

Table 1. Results of Device Simulations for Optical Coatings on Thin Film InP

InP layer thickness	0.5 μm			1 μm			2 μm		
Material	Bare InP	Si$_3$N$_4$	TiO$_2$ NCs	Bare InP	Si$_3$N$_4$	TiO$_2$ NCs	Bare InP	Si$_3$N$_4$	TiO$_2$ NCs
J_{sc} (mA/cm^2)	20.70	24.82	26.10	21.78	28.86	30.47	21.25	27.00	28.85
V_{oc} (V)	0.902	0.906	0.908	0.901	0.908	0.909	0.891	0.899	0.901
FF (%)	85.9	86.1	86.1	83.3	83.8	83.9	80.1	80.2	80.2
η (%)	16.04	19.36	20.41	16.35	21.96	23.24	15.16	19.47	20.85

Table 1 shows the results of device simulations for InP solar cells with varied active layer thicknesses and optical coating structures. These parameters were calculated from electrical simulations using generation rate profiles similar to those from Figs. 4(a)-4(c) as inputs. Note the significant increase in the short-circuit current density and efficiency between the thinnest active layer and the two thicker configurations. Additionally, for all cases the optimized TiO$_2$ NCs perform substantially better than the Si$_3$N$_4$ ARC.

5. Conclusions

In conclusion, we have described high efficiency InP solar cells that use a periodic array of TiO$_2$ nanophotonic resonant structures to enhance their optoelectronic performance. Geometric optimizations utilizing solar-weighted reflectance as a figure of merit and spectrally resolved reflectance studies have shown that these structures, when properly optimized, can have a solar-weighted average reflectance of 1.3%, outperforming traditional antireflection coatings. Additionally, these nanostructures do not require modification of the absorber layer, which may help reduce complexity and cost, while simultaneously limiting the negative effects of increased surface recombination. These nanostructured optical coatings can push the efficiency of InP cells to > 23%, taking advantage of the coupling between Mie resonance and thin-film interference effects. By using inexpensive industrial fabrication processes such as nanoimprint lithography, these types of structures can be fabricated on other high-index substrates, thus continuing to push the limits of photovoltaic performance.

Acknowledgments